A Square Pulse Thermoreflectance Technique for the Measurement of Thermal Properties

Yuzhou Wang[1] · **Vinay Chauhan[2]** · **Zilong Hua[1]** · **Robert Schley[1]** · **Cody A. Dennett[1]** · **Daniel Murray[1]** · **Marat Khafizov[2]** · **Geoffrey Beausoleil II[1]** · **David H. Hurley[1]**

Abstract

We report on a laser-based square pulse thermoreflectance (SPTR) technique for the measurement of thermal properties for a wide range of materials. SPTR adopts the pump-probe thermoreflectance principle to monitor the evolution of local temperature after square pulse excitation. The technique features a compact setup, high spatial resolution, and fast data collection. By comparing the acquired SPTR signals with a continuum heat transfer model, material thermal properties can be obtained. Taking advantage of various spot sizes and modulation frequencies, SPTR can measure both the thermal diffusivity and thermal conductivity of poorly to moderately conductive materials and the thermal conductivity of conductive materials with satisfactory accuracy, with potential to be applied to more conductive materials. The technique was validated on three materials: fused silica, single crystal CaF_2 and single crystal nickel (with conductivities ranging from 1 $W \cdot m^{-1} \cdot K^{-1}$ to 100 $W \cdot m^{-1} \cdot K^{-1}$) with typical measurement errors of 5 % to 20 %. The leading sources of error have been identified by Monte Carlo simulations, and the primary limitations of SPTR are discussed. The compact, fiberized platform we describe here will allow instruments based on this methodology to be deployed in complex, multi-analytical environments for the type of high-throughput correlative analyses that are key to materials design and discovery.

✉ Yuzhou Wang
yuzhou.wang@inl.gov

✉ Zilong Hua
zilong.hua@inl.gov

✉ David H. Hurley
david.hurley@inl.gov

[1] Idaho National Laboratory, Idaho Falls, ID 83415, USA

[2] Department of Mechanical and Aerospace Engineering, The Ohio State University, Columbus, OH 43210, USA

1 Introduction

Understanding the thermal properties of materials is of great importance for emerging energy technologies ranging from thermoelectrics to advanced batteries, fuel cells, and nuclear materials [1–5]. In these applications, temperature control is key functionality for prolonging the service life of essential components. The thermal properties of these energy materials can change significantly depending on composition, structure/microstructure, and aging/usage time [6–10]. It is imperative to understand how heat is transported under various conditions to develop new materials that can meet the increasing demands imposed by these technologies, ranging from advanced thermoelectric to microelectronic materials. Currently, several research programs are underway to accelerate new material discovery through the synergistic integration of experiment and theory [11, 12]. These endeavors call for large matrices of thermal testing, which requires new techniques that can characterize a material's thermal properties in a nondestructive, high-resolution, and high-throughput fashion, allowing relationships between composition, microstructure, and properties to be established in a short time.

Traditional steady-state methods and laser flash analysis are the two most commonly used techniques to evaluate thermal properties [13]. Although these conventional techniques have been proven successful on many materials, they require predefined sample geometry, access to the backside of samples, and exhibit limited spatial resolution and are relatively slow due to serial-type data acquisition. Laser-based pump-probe thermoreflectance techniques have been demonstrated as powerful tools for the evaluation of thermal properties for a wide range of materials [14–18]. Thermoreflectance techniques rely on the effect that the optical reflectance is directly proportional to the surface temperature under small temperature changes. In these techniques, a material is heated by an intensity modulated laser (i.e., pump laser), and the temperature-induced reflectivity change at the sample surface is recorded using a second laser (i.e., probe laser). The excitation and detection are conducted on the same side of the material, and there are few restrictions on sample size or shape. By fitting the experimental data of the amplitude and phase profiles of the probe beam to a continuum heat transfer model, thermal transport properties, i.e., thermal conductivity, thermal diffusivity, and interfacial thermal resistance, can be extracted.

Combining thermoreflectance techniques with other characterization methods offers a promising solution for the high-throughput screening of new materials. In addition to chemical and microstructural properties from popular methods, such as Raman spectroscopy and electron microscopy, thermoreflectance techniques provide complementary information on thermophysical properties especially important for energy applications. The configuration of collinear source and receiver and small laser spot sizes allow for micrometer-resolution spatial mapping of thermal properties without the need to access the back side of samples [6,

19, 20]. Rapid screening combined with chemical and microstructural analysis will provide materials scientists with a powerful tool for developing new materials. Moreover, the interrogation volumes of these microstructure and thermophysical techniques are comparable, enabling a direct correlation between measurement results. The integrated technique described here would accelerate new material discovery by providing straightforward connections between material microstructure, chemical, and thermophysical properties through short, nondestructive analysis.

Various techniques based on the thermoreflectance principle have been developed to study thermal properties of bulk materials and thin films. Using ultrafast lasers, the time domain thermoreflectance (TDTR) technique is able to track thermal transport across nanostructures and in multiple directions [14, 21–25]. In frequency domain thermoreflectance (FDTR), both continuous wave (CW) and ultrafast pulsed lasers can be utilized to measure the phase lag of a thermal wave relative to the modulation wave to extract thermal properties [26–28]. In spatial domain thermoreflectance (SDTR), the relative position of pump and probe beams are swept to study heat dissipation in isotropic and anisotropic materials [29–32]. A steady-state thermoreflectance (SSTR) method has also been developed to measure thermal properties by monitoring the temperature rise under different excitation powers and spot sizes [33].

Recently, a square pulse thermoreflectance (SPTR) technique was proposed to study local heat transport in uranium-nitride/silicide nuclear fuels [19]. This technique utilizes a train of square wave pump pulses to periodically heat a sample surface and a second probe beam to record the optical reflectance that is proportional to the temperature change as a function of time. SPTR possesses the advantages of thermoreflectance techniques, such as high spatial resolution (orders of μm) and short measurement times (order of minutes). Although the time resolution of SPTR is several orders of magnitude lower than TDTR, limiting its applications in certain studies such as monitoring the thermal diffusion in the window of nanoseconds [34], SPTR system is more cost effective and compact, allowing for possible integration with other instruments to provide a multifaceted tool for material characterization and screening [35–37]. Compared to FDTR that collects and analyzes the phase profile of the thermal wave using a lock-in amplifier, SPTR collects the amplitude profile using an oscilloscope, of which the temperature response due to external excitation can be visually observed. These advantages make SPTR an ideal entry point for researchers and engineering students to measure and understand thermal transport phenomena. With the capability demonstrated and validated in [19], some knowledge gap remains when applying SPTR to measure thermal properties, regarding the impacts of sample thermal properties, interfacial resistance, and experimental parameters, such as laser spot size, transducer film thickness, and modulation frequency, on the measurement results.

In this work, the SPTR technique is further developed and we discuss in detail how to most effectively utilize SPTR to measure material thermal properties. The paper is organized in the following manner: First, the details of experimental implementation and the theory of measurement are described. Next, we investigate the appropriate experimental settings to extract thermal properties based on sensitivity

analysis. Particularly the similar sensitivities to the sample's thermal properties and interfacial thermal resistance on conductive materials bring challenges to determining each property separately. Measurement results on fused silica (f-SiO$_2$), calcium fluoride (CaF$_2$), and nickel (Ni) are presented and compared with literature values to demonstrate the method's accuracy and reliability. Finally, sources of errors and limitations of the technique are discussed.

2 Experimental Setup and Theory

2.1 Experimental Setup

The experimental setup of SPTR has been introduced before and is briefly described here (Fig. 1) [19, 29]. The pump and probe beams are derived from optical fibers coupled to two CW diode lasers (Coherent Obis) with wavelengths at 660 nm and 532 nm, respectively. In a typical thermoreflectance experiment, a thin film of metal (e.g., Au, Al) is deposited on the sample surface to provide extra boundary conditions and act as a transducer to ensure a large thermoreflectance coefficient and high optical absorption. Gold was chosen in this work for its large thermoreflectance coefficient at 532 nm [38].

Both laser beams are coupled to optical fibers and subsequently launched, directed to, and focused on the sample surface by dichroic mirrors and a microscope objective lens. The power of laser beams reaching the sample surface is typically on the order of 1 mW and is adjusted to avoid a large DC temperature rise. The sample is placed on a high precision vertical stage. The polarization-controlled probe beam
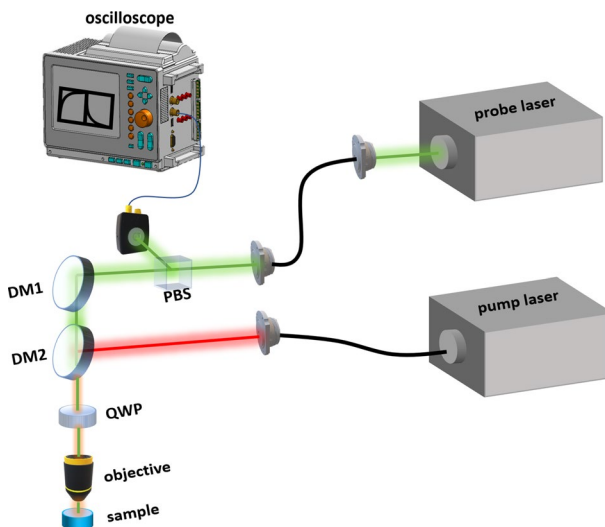

Fig. 1 Design diagram of the experimental setup for SPTR measurement (*DM* dichroic mirror, *QWP* quarter waveplate, *PBS* polarizing beam splitter)

reflected from the sample surface is directed to a photodiode (Thorlabs PDA36A2 with the amplification setting of 20 dB, corresponding bandwidth 1 MHz) through a polarizing beam splitter and the resulting signal is captured by a high-speed digital oscilloscope (Agilent DSO6014A, bandwidth 100 MHz).

The pump beam amplitude is digitally modulated to have a 50 % duty cycle square wave. Two objective lenses with magnifications of 50× and 20× are used in this work. By varying the laser spot size in the measurements, it is possible to measure additional thermal properties besides thermal diffusivity, as will be discussed later. The $1/e^2$ spot radii were measured to be 1.37 μm and 3.17 μm for both pump and probe beams under the 50× and 20× objectives, respectively. The measured signal is averaged over 8000 cycles by the oscilloscope to improve the recorded signal to noise ratio and to keep the time of measurement for one point to less than one minute.

2.2 Theory

After the surface temperature signal is recorded by the oscilloscope, the amplitude profile is compared to a continuum heat transfer model to generate the best-fitting thermal properties using least squares regression. The model describes the surface temperature of a multilayer structure under a square wave thermal excitation. First, we decompose square wave $x(t)$ to the sum of an infinite number of odd harmonic waves [19]

$$x(t) = \sum_{n=-\infty}^{\infty} \frac{\exp(i\omega t(2n-1))}{2n-1}, \tag{1}$$

where t is time and ω is the fundamental harmonic frequency. For each harmonic excitation, the surface temperature response of a two-layer system in the frequency domain has been derived previously and is given by [22, 39]

$$H(\omega) = \frac{Q}{2\pi} \int_0^\infty dp\, W(\omega,p) exp\left(\frac{-p^2\left(r_0^2 + r_1^2\right)}{8}\right)p, \tag{2}$$

where

$$W(\omega,p) = \frac{\frac{\gamma_s}{\gamma_f}m + \gamma_s R_{th} + 1}{\gamma_s + \gamma_f \gamma_s R_{th}m + \gamma_f m}. \tag{3}$$

The definition of the parameters in the above equations are listed in Table 1. The subscript represents either substrate (s) or transducer (f).

The resulting temperature response in the time domain under a square wave excitation is obtained by taking the inverse Fourier transform of $H(\omega)$ and summing the harmonics [19]

$$T(t) = \sum_{n=-N}^{N} H(\omega(2n-1))\frac{\exp(i\omega t(2n-1))}{2n-1} \text{sinc}\left(\frac{n}{2N}\right). \tag{4}$$

Table 1 Definition of parameters in the model

Parameter	Definition
r_0 and r_1	$1/e^2$ radius of pump and probe beams
p	Spatial Fourier transform coordinate
Q	Absorbed laser power
k	Thermal conductivity
C	Volumetric heat capacity
D	Thermal diffusivity $\left(D = \frac{k}{C}\right)$
q	Thermal wave vector $q = \sqrt{p^2 + \frac{i\omega}{D}}$
γ	$\gamma = qk$
d_f	Film thickness
R_{th}	Interfacial thermal resistance between the substrate and transducer film
m	$m = \tanh(q_f d_f)$

We find that it is sufficient to take integration limit as $N = 100$ as the amplitudes of higher harmonics are negligible. The last term in Eq. 4 is the Lanczos sigma factor to remove the undesired Gibbs phenomenon (i.e., ringing effect) often observed in signal processing.

When the modulation frequency is close to the bandwidth of the photodetector, high-order harmonics will be filtered out, resulting in the distortion of both the pump and probe signal. To account for this, we need to modify the model to analyze the data of imperfect high frequency square pulses by introducing corrections to Eq. 4:

$$T'(t) = \sum_{n=-N}^{N} H(\omega(2n-1)) \frac{\exp(i\omega t(2n-1))}{2n-1} \mathrm{sinc}\left(\frac{n}{2N}\right) P\exp(i\phi), \qquad (5)$$

where P and ϕ are the amplitude and phase of the correction function, respectively. These parameters depend on the specifics of experimental instruments and frequency. The derivation of these parameters and the impact will be given in the last section and the appendix.

The samples in this work include f-SiO$_2$, CaF$_2$, and Ni. F-SiO$_2$ has a relatively small thermal conductivity (1.38 W·m^{-1}·K^{-1}, 0.83 mm^2·s^{-1}) and represents the lower bound in this study; CaF$_2$ has moderate thermal properties (9.71 W·m^{-1}·K^{-1}, 3.58 mm^2·s^{-1}); and Ni represents energy materials with relatively high thermal conductivity (90.7 W·m^{-1}·K^{-1}, 23.0 mm^2·s^{-1}).

The thermal conductivity of gold films has been found to be very sensitive to the film thickness [40, 41]. To accurately measure this value, BK7 standards were deposited with gold in tandem with the samples of interest. The conductivities of these Au films on BK7, which were co-deposited with the samples, were measured separately using SDTR.

An example SPTR signal is simulated using the model described in Eq. 4 and presented in Fig. 2a. The model parameters are provided in the caption [42]. The
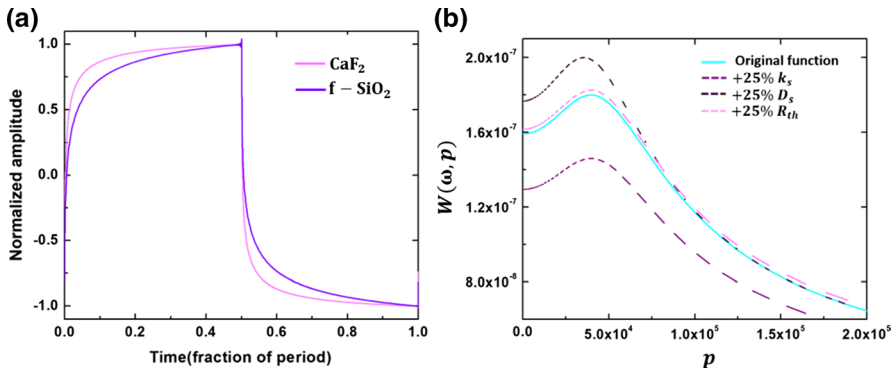
Fig. 2 (a) Theoretical SPTR response on CaF_2 and f-SiO_2 coated with a 36 nm gold transducer film at the modulation frequency of 10 kHz. For these calculations, the interfacial thermal resistance is set to 1×10^{-8} m^2·K·W^{-1}, the film conductivity to 128 W·m^{-1}·K^{-1}, and spot size is 1.37 μm. (b) The function $W(\omega, p)$ simulated on 41 nm gold coated on Ni using a 10 kHz modulation frequency and 50×objective. p is the Fourier transform factor of radial coordinate. The dash lines correspond to 25 % changes to R_{th}, k_s, and D_s

square pulse response is normalized by the maximum amplitude and the length of one cycle. It is noted here that, depending on the length of period or modulation frequency, the surface temperature may or may not reach a steady state at the middle of the cycle. Whether the signal reaches steady state does not impact the results, as the largest sensitivity to thermal properties is provided by the rising/falling sections that promptly follow the incidence/removal of pump pulse as demonstrated later. As soon as the pump laser is turned off, the temperature drops quickly and then slowly returns to minimum level at the end of the period. The rising and falling curves should be identical based on the model. Over the square pulse cycle, the same amount of energy can be imparted to or removed from the system, both of which have the same mathematical expressions except for the sign of Q in Eq. 2.

The shape of the response signal is extremely sensitive to a material's thermal properties. For CaF_2, the observed temperature change is much faster than that of f-SiO_2. This indicates that heat is transported faster in CaF_2 compared to f-SiO_2. Following this logic, one possible application for the SPTR technique is to provide an instant comparison of materials' thermal properties by comparing the rising of amplitude in the time domain (assuming measurements are performed with identical experimental conditions).

3 Sensitivity Analysis

As the model indicates, the temperature response is determined by several parameters (i.e., thermal properties of the transducer film and substrate, modulation frequency, and laser spot). These properties impact the result in a complex manner; thus it is important to investigate each parameter separately to determine optimal

experimental settings and the range of thermal properties that can be evaluated accurately.

For materials with low or moderate thermal conductivities, numerical calculation indicates that Eq. 3 can be simplified to the following form

$$W_L(\omega, p) \approx \frac{1}{\gamma_s} \times \frac{1}{1 + m\left(\gamma_f R_{th} + \frac{\gamma_f}{\gamma_s}\right)}. \tag{6}$$

For a thermally thin transducer film with a thickness much smaller than the thermal diffusion length, $\sqrt{2D_s/\omega}$, the parameter m approaches zero such that terms containing m can be omitted. In this limit, $W_L(\omega, p)$ is thus solely determined by substrate thermal properties.

For materials with high thermal conductivity (close to or above 100 W·m^{-1}·K^{-1}), the simplifications taken to derive Eq. 6 no longer hold and Eq. 3 can be alternatively transformed to the following form

$$W_H(\omega, p) \approx \frac{1 + \gamma_s R_{th}}{\gamma_s + \gamma_s \gamma_f R_{th} m}. \tag{7}$$

For thermally thin films, the terms containing m can also be safely ignored to obtain

$$W_H(\omega, p) \approx R_{th} + \frac{1}{\gamma_s}. \tag{8}$$

In this limit the film doesn't impact the resulting time-dependent profile. However, the interfacial resistance cannot be ignored and must be considered when extracting material thermal properties. When the modulation frequency increases, the thermal diffusion length will decrease and approach the transducer film thickness such that $W(\omega, p)$ will be more coupled to both the film and interfacial properties.

To understand the impact of spot size on the SPTR signal, we plot the simulated function $W(\omega, p)$ for 41 nm gold coated Ni under 10 kHz modulation frequency in Fig. 2b. In addition, the same function with 25 % variations to R_{th}, k_s, or D_s are also presented in the same figure. From Fig. 2b, the impact of D_s is confined to the region where the spatial Fourier parameter p is less than 1×10^5, whereas R_{th} and k_s impact the response $W(\omega, p)$ over a very broad range of p. According to Eq. 2, the frequency response $H(\omega, p)$ is obtained by convolving $W(\omega, p)$ with Fourier transformed Gaussian spot profile. A large laser spot will reduce the weighting of large p in the integration of Eq. 2, diminishing the impact of film and interfacial resistance while improving the sensitivity to D_s. As a result, it is possible to take advantage of different spot sizes and determine multiple thermal properties of a given, fixed layered structure [16, 33, 39].

To explicitly describe the impact of each parameter ξ, we define a sensitivity function as [29]
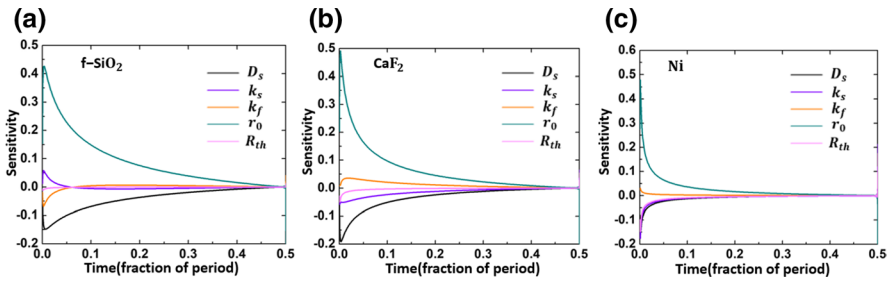
Fig. 3 Sensitivity analysis on f-SiO$_2$, CaF$_2$, and Ni at a modulation frequency of 10 kHz, using the 50× objective. (a) f-SiO$_2$ coated with 36 nm gold; (b) CaF$_2$ coated with 82 nm gold; (c) Ni coated with 41 nm gold

$$S_\xi(t) = \frac{\partial T(t)}{\partial \xi} = \frac{T(\Delta\xi + \xi, t) - T(\xi, t)}{\Delta\xi/\xi}. \tag{9}$$

The function $S_\xi(t)$ for 36 nm gold coated f-SiO$_2$, 82 nm gold coated CaF$_2$, and 41 nm gold coated Ni are presented in Fig. 3, where ξ includes thermal diffusivity, D, and conductivity, k, for both film and substrate, as well as laser spot radius and interfacial thermal resistance R_{th} between the transducer film and substrate. These film thicknesses are chosen to ensure large sensitivity to substrate thermal properties based on Fig. 4 and related discussions in the following analysis. The interfacial thermal resistance is set to 1×10^{-8} m^2·K·W^{-1}, typical in the range of previous measurements [43]. The thermal conductivities of transducer films on f-SiO$_2$, CaF$_2$, and Ni are 128 W·m^{-1}·K^{-1}, 133.6 W·m^{-1}·K^{-1}, and 130.9 W·m^{-1}·K^{-1}, respectively, based on SDTR measurements. Only half a cycle is presented since the second half carries the same information based on Fig. 2a.

As is clearly illustrated in Fig. 3, most of the changes happen during the fast-rising section of the square wave period (before one-tenth of a period). In addition, the spot size has a very large impact on the overall result and should be measured accurately [28, 33]. In fact, for most experimental configurations, spot size has a dominant impact on the temperature response and is the most important experimental
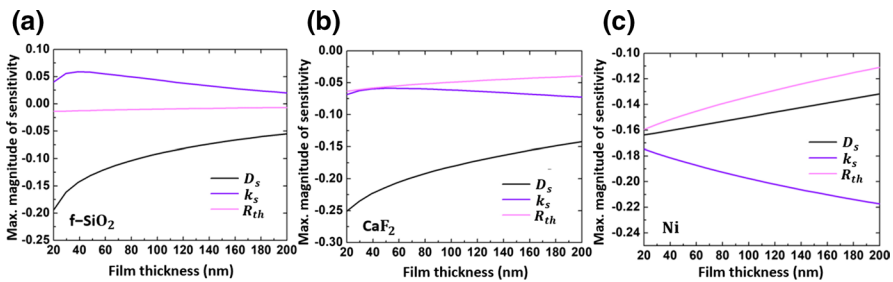

Fig. 4 Maximum magnitude of sensitivity function S_ξ for thermal conductivity, diffusivity, spot size, and interfacial resistance vs gold film thickness (at 10 kHz frequency and using the 50× objective). (a) f-SiO$_2$, (b) CaF$_2$, (c) Ni

parameter as well as the largest source of error. The rise time τ of the temperature response can be roughly approximated by $\tau = \frac{C_f r^2}{3k_s}$ [19]. Only the spot radius has a parabolic relationship to τ whereas the rest of material properties have a first-order relationship. An inaccurate spot size could induce large error to the fitting results; this dependence will be discussed in detail in the final section.

For f-SiO$_2$ and CaF$_2$, the transducer films are thermally thin such that they only have a limited impact on the measured response. Besides spot size, substrate thermal diffusivity has the largest impact. The sensitivity to the substrate thermal conductivity is low but non-negligible, as the convolved spot size is comparable with thermal diffusion length, resulting in some degree of radial thermal transport [39]. Thus, it is difficult to distinguish thermal conductivity and diffusivity from a single SPTR measurement. For Ni, the impact of the interface increases significantly in accordance with Eq. 8. As Fig. 3c shows, sensitivities of interfacial thermal resistance and substrate conductivity have comparable amplitudes over most of the period. It can be explained through a "serial thermal resistance" model [44], by considering both the film and substrate as two thermal resistances serially connected by the interfacial resistance. Compared to other substrates used in this study, the larger thermal conductivity of Ni makes its thermal resistance significantly smaller and become comparable to the interfacial thermal resistance. Therefore, the extraction of interfacial thermal resistance is only possible on Ni, if its impact on the signal can be separated from the one from the Ni substrate thermal conductivity.

To investigate the impact of transducer film thickness on the sensitivities of thermal properties, we calculate the maximum magnitude of the sensitivity function S_ξ for our test samples and for film thicknesses in the range of 20 nm to 200 nm (Fig. 4). This range of film thicknesses is typical of thermoreflectance measurements. The thermal conductivity of gold film is based on the interpolation of results independently measured on gold films with various thicknesses. The modulation frequency is set to 10 kHz and the objective magnification is 50×. The maximum magnitude of sensitivity S_ξ is defined as the value with the largest absolute magnitude of a sensitivity function in a single period. For example, the maximum magnitude of sensitivity S_{D_s} in Fig. 3a is -0.15. Other controlled parameters, such as the thickness and thermal conductivity of transducer film, can be determined separately and are not discussed here. In the subsequent discussion, unless explicitly stated, the absolute values of sensitivity function are used. However, the sign of S_ξ is also important as it indicates the correlation between different properties.

For f-SiO$_2$ and CaF$_2$, the impact of film thickness is greatest on S_{D_s} according to Fig. 4a and b. The sensitivity of thermal diffusivity decreases significantly for a thicker gold film. The sensitivity of interfacial thermal resistance is minimally impacted for f-SiO$_2$ and slightly decreases for CaF$_2$. For f-SiO$_2$, the sensitivity S_{k_s} increases until 50 nm and then starts to decrease. In contrast, the sensitivity S_{k_s} of CaF$_2$ decreases at first and then slowly increases with the film thickness. The S_{k_s} of f-SiO$_2$ and CaF$_2$ have opposite signs. To measure the thermal properties of f-SiO$_2$, film thickness around 40 nm corresponding to large sensitivities of k_s and D_s is appropriate. As for CaF$_2$, in addition to the sensitivities of thermal properties,

the impact of interface needs to be minimized. Therefore, we chose film thickness around 90 nm in this study.

From the results in Fig. 4c, the impact of film thickness on Ni is generally limited. The sensitivity S_{k_s} increases slightly and sensitivity S_{D_s} decreases slightly with an increasing film thickness. For these reasons, on highly conductive materials, film thicknesses smaller than 100 nm are appropriate to ensure a large sensitivity to substrate thermal properties. To minimize the impact of substrate on the signal, the thickness of transducer should be at least on the order of optical penetration depth for both pump and probe light in Au.

To further investigate the impact of spot size and modulation frequency on the sensitivities of thermal properties, we calculate the maximum magnitude of sensitivity function S_ξ for the aforementioned three samples in the frequency range of 10^2 to 10^5 Hz and under two microscope objectives and present the results in Fig. 5. The lower frequency limit is set here by the detector noise level while the higher boundary is limited by the detector bandwidth [45].
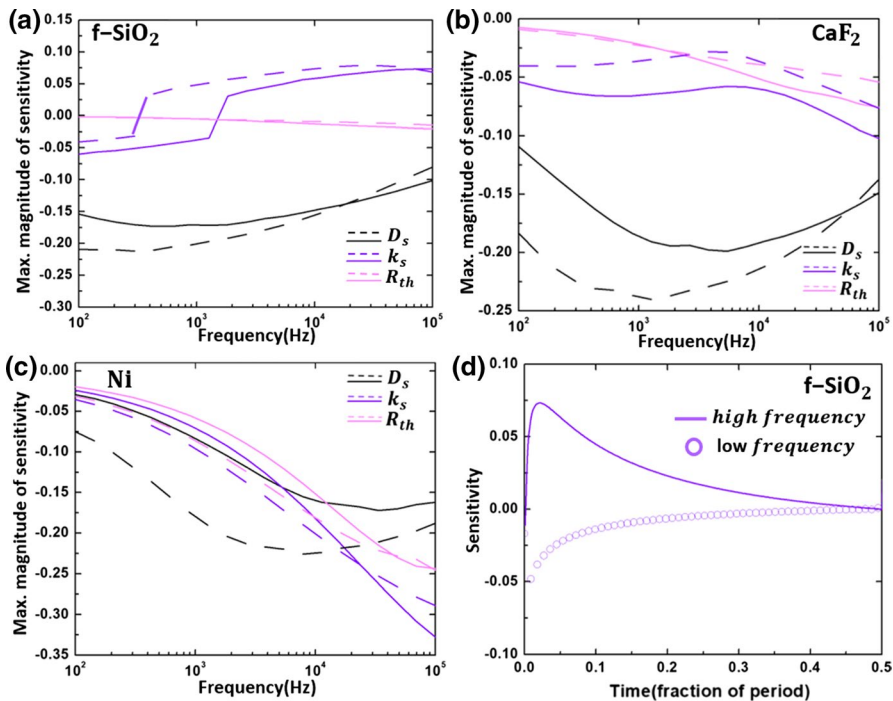

Fig. 5 Maximum magnitude of sensitivity function S_ξ for thermal conductivity, diffusivity, and interfacial thermal resistance vs modulation frequency (magnifications of objective are 50× (solid line) and 20× (dash line)). (a) 36 nm gold coated f-SiO$_2$, (b) 82 nm gold coated CaF$_2$, (c) 41 nm gold coated Ni, and (d) shapes of sensitivity function S_{k_s} for f-SiO$_2$ at low (100 Hz) and high (100 kHz) frequency. The small kinks in some curves are numerical artifacts; the true peak position of S_ξ may not be captured by the simulation due to its sharpness

According to Fig. 5, for larger spot sizes, the sensitivity to substrate thermal diffusivity is generally improved while the sensitivities to all other parameters are suppressed, in agreement with the conclusions of Fig. 2b. For materials with poor thermal conductivity, such as f-SiO$_2$, the impact of the interface is limited over a broad range of frequencies and can be safely ignored in the data analysis. The impact for thermal diffusivity is the strongest near 1 kHz for the 50× objective or 400 Hz for 20× objective. These frequencies also correspond to the smallest sensitivity to thermal conductivity. Far away from these frequencies the sensitivity to conductivity is improved whereas that of thermal diffusivity drops, thus bringing their sensitivities to a comparable level. The abrupt crossover of the maximum magnitude for S_{k_s} from negative to positive value around 1 kHz in Fig. 5a is due to the change of S_{k_s} shape illustrated in Fig. 5d. At low frequencies, the values of S_{k_s} are negative (symbols in Fig. 5d); in contrast, the shape of S_{k_s} is flipped around the x axis at a high frequency and the maximum magnitude becomes positive (solid line in Fig. 5d).

For moderately conductive materials such as CaF$_2$, interfacial thermal resistance only affects the SPTR temperature profile on the higher end of the considered frequency range. Therefore, to reduce its influence when measuring material thermal properties, it is sufficient to avoid high frequencies. The frequencies corresponding to the largest and smallest sensitivities to thermal diffusivity and conductivity increase compared to those of f-SiO$_2$. Finally, for very conductive materials such as Ni, the sensitivity of interface has a comparable amplitude to those of thermal properties over a broad range of frequency and should be accounted for when extracting material thermal properties.

We recall that the primary objective of this work is to develop a reliable methodology to measure substrate thermal properties. The above sensitivity analysis suggests that the measurement accuracy depends on the ability to properly account for the interfacial thermal resistance. One single SPTR measurement is not sufficient to determine all of the three unknown thermal properties (D_s, k_s and R_{th}) that impact the temperature evolution. Some combinations of two thermal properties may be determined by analyzing several measurements in different frequency ranges. The determination of all three thermal properties proves to be challenging for the current SPTR configuration.

Furthermore, the sensitivity analysis in Figs. 3, 4 and 5 indicates that the experimental settings should be chosen based on the specific material properties to ensure the largest sensitivity to the interested properties and the smallest sensitivity to the undesired ones. A large sensitivity corresponds to small errors when extracting thermal properties from experimental data using a multilayer thermal transport model. This especially applies to the experimental settings on poorly or moderately conductive materials to ensure the sensitivity of interfacial thermal resistance is negligible. If the interfacial thermal resistance has a non-negligible sensitivity in a wide range of settings, for example on Ni, it is appropriate to choose settings that have enough sensitivity to the material thermal properties and interfacial thermal resistance so that both quantities can be determined accurately.

The optimal experimental settings based on the material thermal properties are summarized in Table 2. For a completely unknown material, thermal properties can first be roughly estimated based on the method of Fig. 2a by comparing the

Table 2 Optimal experimental settings to extract thermal properties

Material thermal conductivity	When heat capacity is known	When heat capacity is unknown
$\mathcal{O}$ (1 W·m⁻¹·K⁻¹)	Large spot size (20×obj.) and thin transducer (<30 nm); frequency is chosen based on sensitivity analysis (generally below 1 kHz)	Moderate transducer thickness (30 nm < d_t < 100 nm); (a) large spot (20×obj.) and low frequency (<1 kHz), or (b) small spot (50×obj.) and high frequency (>1 kHz)
$\mathcal{O}$ (10 W·m⁻¹·K⁻¹)	Large spot size (20×obj.) and thin transducer (<30 nm); frequency is chosen based on sensitivity analysis (generally below 1 kHz)	Moderate transducer thickness (30 nm < d_t < 100 nm); (a) large spot (20×obj.) and low frequency (<1 kHz) or (b) small spot (50×obj.) and moderate frequency (1 kHz < f < 10 kHz)
$\mathcal{O}$ (100 W·m⁻¹·K⁻¹)	Small to moderate film thickness (<100 nm); (a) large spot (20×obj.) and low frequency (<10 kHz), or (b) small spot (50×obj.) and high frequency (>20 kHz)	n/a

Two settings are given for some cases that have distinct sensitivities for interested parameters

temperature rise time with tabulated results. Afterwards, experimental settings may be shifted based on the recommendations below to make high-confidence measurements of the properties of interest.

If the material heat capacity is already known, the number of unknown thermal parameters is reduced to two, namely D_s and R_{th}. The thermal diffusivity of f-SiO$_2$ and CaF$_2$ can be directly obtained from a single measurement of appropriate spot size and frequency that correspond to a large sensitivity to D_s and very small sensitivity to R_{th}, such as 1 kHz and 20× objective in Fig. 5b. Moreover, the gold film should be thin enough to ensure enough sensitivity to D_s according to Fig. 4a and b.

On the other hand, if heat capacity is unknown, we can take advantage of the distinct sensitivities at different settings and combine two measurements to extract both D_s and k_s. The method to analyze these sets of data is analogous to the simultaneous determination of several parameters in FDTR and TDTR [16, 39]. Although many combinations of material properties can explain the experimentally obtained temperature response under each experimental setting, the true material properties should be able to generate temperature responses from modeling that can satisfactorily match the experimental results of all combinations of spot sizes and frequencies. The experimental settings should be carefully selected such that the ratios of sensitivities between D_s and k_s are distinct for both cases while maintaining as low a sensitivity to R_{th} as possible. As illustrated in the experimental validation section, the distinct ratios of sensitivity allow for the D_s vs k_s curves of two data sets to intersect at a clear point. This can be conveniently achieved by adjusting spot size and modulation frequency based on the sensitivity analysis in Fig. 5. The thickness of the applied gold transducer film is not convenient to change in experiments compared to spot size or frequency, and therefore should be selected in the range where sensitivities of D_s and k_s have comparable and large amplitudes.

For highly conductive materials, R_{th} needs to be considered at most frequencies and heat capacity needs to be known a priori to eliminate one unknown quantity. Two measurements are required to resolve both D_s and R_{th}. The experimental settings should be carefully selected so that in one setting, the sensitivity ratio of D_s and R_{th} is distinct from that in the other setting. A large film thickness should

Table 3 Measured and literature values of thermal conductivity (k) and thermal diffusivity (D)

Samples (transducer thickness)	Literature values [29, 42, 46]		Heat capacity is known		Heat capacity is unknown	
	K (W·m^{-1}·K^{-1})	D (mm^2·s^{-1})	K (W·m^{-1}·K^{-1})	D (mm^2·s^{-1})	K (W·m^{-1}·K^{-1})	D (mm^2·s^{-1})
f-SiO$_2$ (36 nm)	1.38	0.83	1.38 ± 0.51	0.83 ± 0.31	1.63 ± 0.52	0.82 ± 0.26
CaF$_2$ (82 nm)	9.71	3.58	10.54 ± 1.39	3.89 ± 0.51	8.81 ± 1.76	4.10 ± 0.82
Ni (41 nm)	90.7	23.0	77.46 ± 14.41	19.66 ± 3.66	n/a	n/a

be avoided as both the sensitivities of D_s and R_{th} decrease with film thickness, as shown Fig. 4c.

4 Experimental Validation

In this section we validate the SPTR technique on several materials listed in Table 3. Validation measurements are separated into two categories. First, we focus on measurements of materials where the heat capacity is known. Second, we evaluate thermal properties when heat capacity is unknown. Ten measurements were taken in each case and the standard deviation between this set of measurements was taken as the ultimate error.

4.1 Measuring Materials with Known Heat Capacity

There are many established means to obtain the heat capacity of a material of interest, such as differential scanning calorimetry and calculations from the Kopp–Neumann law and phase field methods [46]. Oftentimes heat capacity is not impacted much by sample size or small microstructural variations and can be taken directly from literature values [46, 47]. In such cases, a confident a priori estimate of the heat capacity reduces the unknown thermal properties and simplifies the ultimate determination of D_s.

Test samples for the validation of the SPTR method were prepared for f-SiO$_2$, CaF$_2$, and Ni. The thicknesses of the gold transducer films deposited on f-SiO$_2$, CaF$_2$, and Ni samples are 36 nm, 82 nm, and 41 nm, respectively. These films ensure a large sensitivity to D_s according to Fig. 4a–c. Their thermal conductivities were measured to be 128 W·m^{-1}·K^{-1}, 133.6 W·m^{-1}·K^{-1}, and 130.9 W·m^{-1}·K^{-1}, respectively.

For poorly or moderately conductive materials, the thermal diffusivity can be straightforwardly calculated in the frequency range where the impact of interface thermal resistance is negligible. To measure the thermal diffusivity of f-SiO$_2$, we chose a 20× objective and 400 Hz to take advantage of the corresponding large D_s sensitivity. For CaF$_2$, we chose a 20× objective and 1 kHz for the high sensitivity to D_s. A typical value in the range of previously measured thermal resistance between metals and dielectrics was set for the interfacial thermal resistance, for example, $R_{th} = 1 \times 10^{-8}$ m^2·K·W^{-1}, which has limited impact as the model indicates [43].

The experimental and model fitting results are presented in Fig. 6a and b. We find a very good agreement between the experiment and the model. The fitting values of substrate diffusivity are 0.83 ± 0.31 mm^2·s^{-1} and 3.89 ± 0.51 mm^2·s^{-1} for f-SiO$_2$ and CaF$_2$, respectively. Taking literature values of heat capacity, their thermal conductivities are calculated to be 1.38 ± 0.51 W·m^{-1}·K^{-1} and 10.54 ± 1.39 W·m^{-1}·K^{-1}. These values agree closely with previously reported thermal properties as shown in Table 3. The larger error associated with SPTR measurement on f-SiO$_2$ is attributed to Au film agglomeration [40].
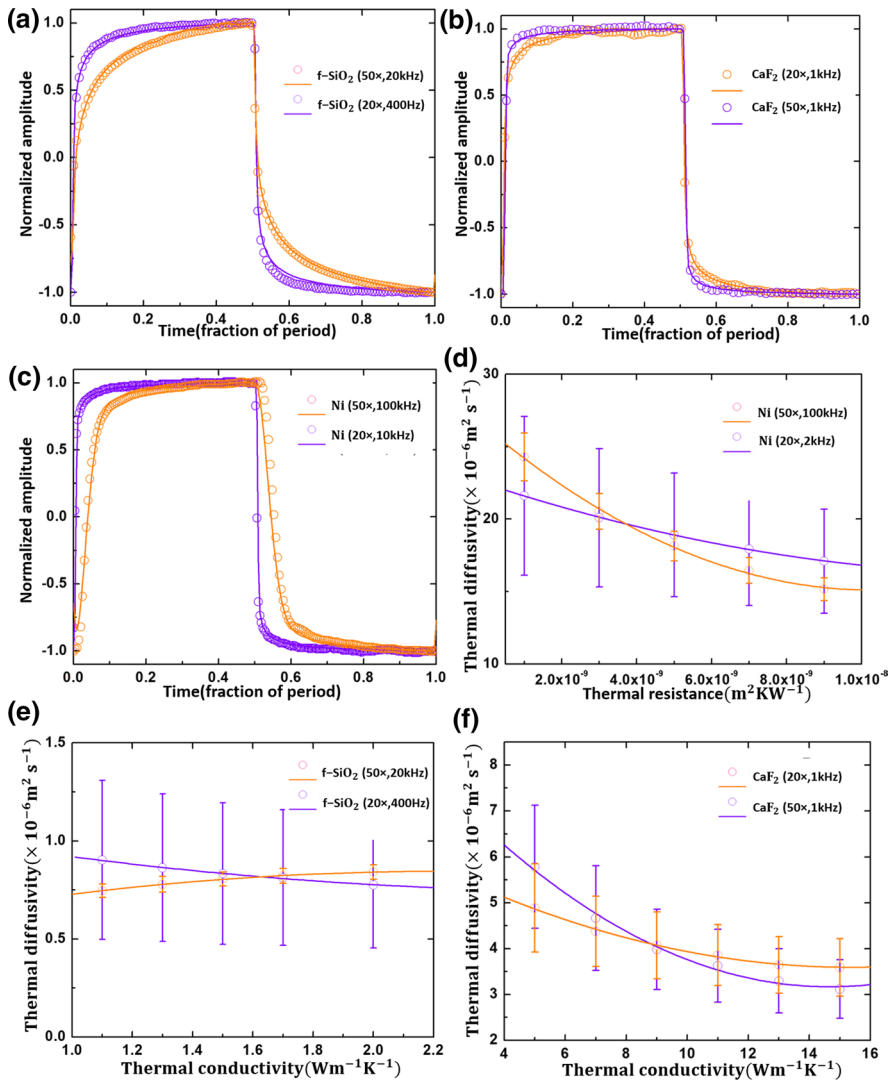
Fig. 6 Experimental and model fitting results. Open circles correspond to the experimental result, and a solid line is the model result. (a) f-SiO$_2$ coated with 36 nm gold, 20× objective, 400 Hz (purple) and 50× objective, 20 kHz (orange); (b) CaF$_2$ coated with 82 nm gold, 50× objective, 1 kHz (purple), and 20× objective, 1 kHz (orange); (c) Ni coated with 41 nm gold, 20× objective, 2 kHz (purple), and 50× objective, 100 kHz (orange); (d) R_{th} vs D_s curves for two data sets measured on Ni sample; (e) k_s vs D_s curves for two data sets measured on f-SiO$_2$ sample; (f) k_s vs D_s curves for two data sets measured on CaF$_2$ sample

To illustrate the large errors originating from inappropriate experimental settings, we also conducted measurements on f-SiO$_2$ with parameters deliberately chosen to reduce the sensitivity to the desired thermal properties. Here, we used a

large film thickness (203 nm), 20× objective, and 100 kHz frequency to measure the thermal conductivity assuming the heat capacity is known. According to the analysis in Figs. 4 and 5, the sensitivity of thermal diffusivity is very small such that an inaccurate result is expected. This is confirmed by the measurement result which yields a thermal conductivity of 2.16 W $\pm 0.52 \cdot \mathrm{m}^{-1} \cdot \mathrm{K}^{-1}$ on f-SiO$_2$ with inappropriate settings.

Next, the thermal diffusivity of Ni is evaluated. Although the film (41 nm) is thermally thin compared to its thermal diffusion length and the spot size is large when using a 20× objective, the analysis from Eq. 8, as well as Fig. 5c, indicates that the interface cannot be ignored for materials with large thermal conductivity. We take the heat capacity and density of Ni as known parameters from literature [42]. With these fixed parameters, the model has two fitting parameters, namely interfacial thermal resistance and substrate thermal diffusivity. To take advantage of the distinct sensitivities in Fig. 5c, two sets of experimental data were taken for 20× objective, 2 kHz and 50× objective, 100 kHz. Next, a range of values for interfacial thermal resistance were applied to the model to fit the experimental data in Fig. 6c, and the corresponding best-fitting thermal diffusivities were obtained. In Fig. 6d, we plot these two sets of data in the same figure. The points are connected by polynomial lines fitted to the experimental data. The crossing point is at $R_{th} = 3.71 \times 10^{-9}$ m$^2 \cdot$K$\cdot$W^{-1}, $D_s = 19.66 \times 10^{-6}$ m$^2 \cdot$s^{-1}. The error at this point was calculated by taking the root mean square of the errors of both parameters at nearby points. Taking the volumetric heat capacity of Ni as $C = 3.94 \times 10^6$ J$\cdot$m$^{-3} \cdot$K^{-1}, the thermal conductivity of Ni is estimated to be $k_s = D_s \times C_s = 77.46$ W$\cdot$m$^{-1} \cdot$K^{-1}. The interfacial thermal resistance is on the same order as previously reported values between gold and other metals [48, 49]. In Fig. 6d, the curve corresponding to 20× objective, 2 kHz has a smaller slope compared to the curve for 50× objective, 100 kHz, which can be explained by the different sensitivities illustrated in Fig. 5c. The ratio of sensitivity between D_s and R_{th} for 20× objective and 2 kHz is larger than that for 50× objective and 100 kHz. As a result, to compensate for the same amount of change in R_{th}, the change of D_s is larger for the case of 50× objective and 100 kHz.

4.2 Measuring Materials with Unknown Heat Capacity

To resolve the thermal conductivity and diffusivity of f-SiO$_2$ and CaF$_2$ when the material heat capacity is unknown, multiple measurements are required to ensure a larger sensitivity to thermal conductivity. For f-SiO$_2$, additional measurements with a 50× objective and 20 kHz frequency were collected; measurements using a 50× objective and 1 kHz frequency were collected as the secondary data set for CaF$_2$. These settings ensure larger sensitivity to thermal conductivity as demonstrated in Fig. 5a and b while the impact of interface is negligible. The film thicknesses also ensure there is enough sensitivity to k_s according to Fig. 4a and b.

The method to extract both k_s and D_s is similar to that of Ni described above. Rather than fitting D_s as a function of R_{th}, it was fitted as a function of thermal conductivity k_s. Examples of fitted model are presented in Fig. 6a and b. The extracted k_s vs D_s results are plotted in Fig. 6e and f. The crossing point for f-SiO$_2$ is $k_s =$

1.63 W·m^{-1}·K^{-1}, and $D_s = 0.82$ mm^2·s^{-1}. For CaF$_2$, the two curves intersect at $k_s = 8.81$ W·m^{-1}·K^{-1}, and $D_s = 4.10$ mm^2·s^{-1}. These results generally have larger errors compared with the values in the previous section due to more unknown properties but are still within the range of errors from measurements taken when the heat capacity is known a priori. From the simultaneous determination of D_s and k_s, we are also able to estimate the volumetric heat capacity C_s.

We note that only the slope of k_s vs D_s curve for f-SiO$_2$ under a 50× objective and 20 kHz frequency is positive while the rest curves have negative slopes. This can be explained by the sensitivity analysis in Fig. 5a. Under these experimental conditions, the sensitivities of k_s and D_s have opposite signs in Fig. 5a, resulting in a positive correlation relation between k_s and D_s when fitting to the data. On the other hand, for the rest curves the sensitivities of k_s and D_s both share the same sign and therefore their properties are negatively correlated.

5 Error Analysis

There are multiple factors that influence the reliability of the SPTR technique. The most critical one is the accurate measurement of laser spot size given the extreme sensitivity evidenced by Fig. 3 where in almost all cases, the sensitivity to spot size is larger than that of the thermal properties. Therefore, determining the spot size for each experimental configuration and objective lens choice is of paramount importance. Even for a well-characterized experiment, when the sample surface is not placed at precisely the focal plane of the objective, the change in spot size will impact the fitting results. For example, for a 50× high magnification objective with a short depth of focus, defocusing by 5 µm can change the projected spot size by 9.5 % and fitting result by 16 %. Therefore, high precision vertical stages with a minimum step size less than 1 µm are recommended for SPTR experimental arrangements.
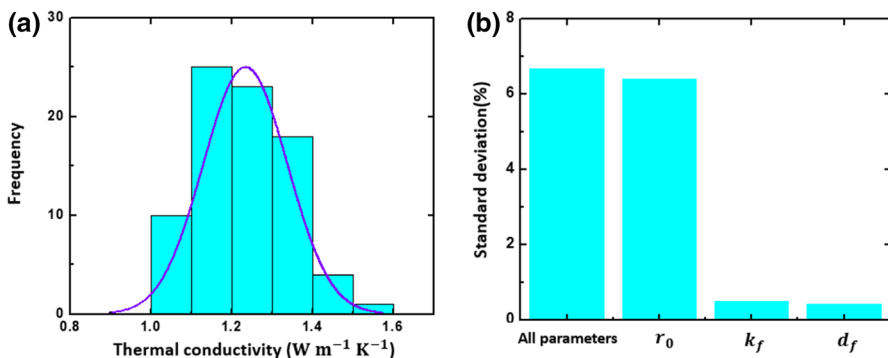

Fig. 7 (a) Histograms of fitted f-SiO$_2$ thermal conductivity from SPTR measurement and fitted normal distribution. (b) Standard deviation of fitted normal distribution with all controlled parameters considered as well as standard deviations when the uncertainty of only one controlled parameter is considered

Additional SPTR measurement was conducted on f-SiO$_2$ under 20× objective and 400 Hz to obtain a statistical distribution of experimental results for an estimation of experimental repeatability. The histogram of fitted thermal conductivity is presented in Fig. 7a. The fitted values of thermal diffusivity follow a normal distribution with a standard deviation of 8.48 %.

To quantitatively estimate the impact of each parameter on the errors associated with thermal properties, we apply a Monte Carlo method to the optimization of the multilayer transport model expressed in Eq. 4 to the experimental data of f-SiO$_2$ at 20× objective and 400 Hz [50, 51]. Each of the "controlled parameters" in this implementation of SPTR can influence the total measurement error, for example the thickness and thermal conductivity of gold film and the convolved pump-probe spot size. To propagate these errors through our forward model, we first experimentally measure uncertainties associated with each control parameter. For spot size, multiple measurements were made to get the value of spot size within a standard deviation of 5 %. The errors associated with the thickness and thermal conductivity of film are estimated to be 2 % and 2.4 %, respectively. Each parameter is assumed to have a normal distribution around its mean value with a standard deviation. We fitted the model with updated controlled parameters to the experimental result repeatedly and obtained the distributions of fitted thermal properties. The resulting standard deviation is 6.67 % that is close to the experimental error determined through statistics of multiple measurements made on a single sample.

Next, the same kind of simulation was repeated when only the finite uncertainty in a single control parameter—spot size, film thickness, or film thermal conductivity—is considered. The resulting errors are summarized in Fig. 7b. The standard deviation produced by the uncertainly of spot size alone is 6.4 % and is comparable to the total standard deviation when all controlled parameters are considered. In contrast, the ultimate uncertainty due to film properties produces around 1 % standard deviation in fitted thermal conductivity; their impact is limited. Based on Fig. 7b, we conclude that the uncertainly of spot size is clearly the largest source of error.

During measurements on f-SiO$_2$, a spatial variation of reflectance was observed, indicating a partially roughened surface on some areas. The measurements reported in this work were taken on an area with a relatively smooth surface. Such surface roughness was not found on thicker transducer films or on the Ni sample. This could be attributed to the agglomeration of deposited metals on insulating oxides at low temperatures [40, 52]. Rough surfaces can significantly impact the reflectance and produce extra errors in the measurement. Therefore, care should be taken when selecting the film thickness on some substrates and avoiding any surface variations. The small spot sizes used in this type of measurement (1–5 μm) make locally avoiding any small surface imperfections reasonably simple.

Errors can also originate from an imperfect square wave excitation and detection. The model expressed in Eqs. 1–4 considers ideal square excitation waves which in practice cannot be achieved due to finite electronic bandwidth. At high frequencies comparable to the laser analog modulation bandwidth and detector bandwidth (500 kHz and 1 MHz, respectively, in this experiment), severe distortion and artifacts of the pump signal have been noticed (e.g., overshoot, undershoot, and signal delays), likely from Gibbs phenomenon. This influence is

severer for SPTR than for FDTR as the square wave is essentially composed of high-order harmonic waves. In practice, we find that at a modulation frequency that is 100 times smaller than the detector bandwidth, the pump pulse can be assumed an ideal square without sacrificing accuracy. However, a large bandwidth often comes at a cost of low gain, which subjects the signal to the system's random noise. Therefore, the selection of modulation frequency not only depends on the sensitivity of interested thermal property, but on instrument parameters as well. The electronic characters of the signal processing system must be properly accounted for before high-quality data may be collected.

Although these phenomena can be partially alleviated by postprocessing, such as the Lanczos sigma factor, assuming an ideal square wave can lead to an inaccurate estimation of conductivity at high frequency [19]. The imperfect square may result in an underestimation of thermal conductivity by a large margin if not properly accounted for. The components (cables, detector, lasers, etc.) of the system have different responses to different harmonics of the fundamental frequencies expressed in Eq. 1. These responses can be conveniently lumped together as a systematic transfer function [19]. As a result, the forward model requires a modification to analyze the data of imperfect high frequency square pulses by introducing corrections to Eq. 4. The resultant Eq. 5 includes P and ϕ as the amplitude and phase of the systematic transfer function, respectively. To derive these parameters of transfer function, we take a Fourier transform of the imperfect square wave pump signal collected directly by the photodetector at each modulation frequency and compare them with the parameters in Eq. 1. The detailed procedure for applying this correction is described in the appendix.

6 Conclusion

In summary, we have demonstrated an SPTR technique to measure thermal properties for a wide range of materials and explored the optimal parameter space for measurements. The SPTR technique relies on the thermoreflectance principle to monitor the amplitude evolution of surface temperature and has advantages compared to other thermophysical characterization techniques, such as ease of operation, fast data acquisition, and compact instrumentation. An analytical model is developed to simulate the thermal transport and its implementation for the analysis of the experimental data to extract thermal properties of interest is demonstrated. A sensitivity analysis demonstrates that the optimal transducer thickness, spot size, and modulation frequency depend on the thermal properties of the sample. We have validated the SPTR technique and found a good agreement with the literature on several reference samples with thermal conductivity in the range of 1 $W \cdot m^{-1} \cdot K^{-1}$ to 100 $W \cdot m^{-1} \cdot K^{-1}$. A measurement error of around 10 %, mostly originating from the uncertainty of the applied laser spot size, is confirmed through a Monte Carlo analysis. Limitations of the technique, particularly high sensitivity to laser spot size and wave distortion at high frequencies, are discussed. This approach provides an attractive solution for applications where

extensive optical alignment is not feasible and offers an opportunity to measure thermal property in a fast and convenient fashion with high accuracy and resolution. The compact and fiberized nature of this and other possible experimental arrangements offers a promising route for the development of multi-analytical tools for expedited materials design and discovery.

Appendix

Ideally, a square wave can be expressed by Eq. 1. Each harmonic has an equal phase of zero and a 1/(2n − 1) amplitude. In an actual experiment, however, the signal is processed by various electrical circuits which inevitably introduce distortions. These distortions are most often frequency dependent. To conveniently capture these effects, we use a lumped transfer function to account for the changes to both amplitude and phase.

First, the imperfect square pulse is measured by removing the short-pass filter normally placed in front of the detector to reject any pump light, shutting down the probe laser, and collecting the pump signal reflected by sample surface using the photodetector.

Next, to derive the transfer function, we express the collected non-ideal square wave as

$$x'(t) = \sum_{m=-\infty}^{\infty} P_m \frac{\exp\left(im\omega t + i\phi_m\right)}{m}, \tag{10}$$

where m are odd integers. Taking advantage of the relation $\int \sin(mt)\sin(nt)dt = \delta_{nm}$ (δ is Kronecker delta function), we can obtain the following relations

$$
\begin{aligned}
P_{m,1} &= \int_0^{\frac{1}{f}} mx'(t) \cos(m\omega t)dt \\
P_{m,2} &= \int_0^{1/f} mx'(t) \sin(m\omega t)dt,
\end{aligned}
\tag{11}
$$

from which the factors P_m and ϕ_m can be expressed as

$$
\begin{aligned}
P_m &= \sqrt{P_{m,1}^2 + P_{m,2}^2} \\
\phi_m &= \mathrm{atan}\left(\frac{P_{m,2}}{P_{m,1}}\right).
\end{aligned}
\tag{12}
$$

Data Availability The data and code that support the findings of this study are available from the corresponding authors upon reasonable request.

Declarations

Conflict of interest The authors declare that they have no conflict of interest.

References

1. D.G. Cahill, P.V. Braun, G. Chen, D.R. Clarke, S. Fan, K.E. Goodson, P. Keblinski, W.P. King, G.D. Mahan, A. Majumdar, H.J. Maris, S.R. Phillpot, E. Pop, L. Shi, Appl. Phys. Rev. **1**, 011305 (2014). https://doi.org/10.1063/1.4832615
2. M. Khafizov, V. Chauhan, Y. Wang, F. Riyad, N. Hang, D. Hurley, J. Mater. Res. **32**, 204 (2016). https://doi.org/10.1557/jmr.2016.421
3. R. Spotnitz, J. Franklin, J. Power Sources **113**, 81 (2003). https://doi.org/10.1016/S0378-7753(02)00488-3
4. W. Liu, Q. Jie, H.S. Kim, Z. Ren, Acta Mater. **87**, 357 (2015). https://doi.org/10.1016/j.actamat.2014.12.042
5. M. Khandelwal, M.M. Mench, J. Power Sources **161**, 1106 (2006). https://doi.org/10.1016/j.jpowsour.2006.06.092
6. S. Huxtable, D.G. Cahill, V. Fauconnier, J.O. White, J.-C. Zhao, Nat. Mater. **3**, 298 (2004). https://doi.org/10.1038/nmat1114
7. D. Hurley, M. Khafizov, S. Shinde, J. Appl. Phys. **109**, 083504 (2011). https://doi.org/10.1063/1.3573511
8. Z. Hua, J. Spackman, H. Ban, Materialia **5**, 100230 (2019). https://doi.org/10.1016/j.mtla.2019.100230
9. X. Bai, M. Tonks, Y. Zhang, J. Hales, J. Nucl. Mater. **470**, 208 (2016). https://doi.org/10.1016/j.jnucmat.2015.12.028
10. M. Khafizov, J. Pakarinen, L. He, D.H. Hurley, J. Am. Ceram. Soc **102**, 7533 (2019). https://doi.org/10.1111/jace.16616
11. J.A. Aguiar, A.M. Jokisaari, M. Kerr, R. Allen Roach, Nat. Commun. **11**, 2556 (2020). https://doi.org/10.1038/s41467-020-16406-2
12. J.J. de Pablo, N.E. Jackson, M.A. Webb, L.-Q. Chen, J.E. Moore, D. Morgan, R. Jacobs, T. Pollock, D.G. Schlom, E.S. Toberer, J. Analytis, I. Dabo, D.M. DeLongchamp, G.A. Fiete, G.M. Grason, G. Hautier, Y. Mo, K. Rajan, E.J. Reed, E. Rodriguez, V. Stevanovic, J. Suntivich, K. Thornton, J.-C. Zhao, npj Comput. Mater. **5**, 41 (2019). https://doi.org/10.1038/s41524-019-0173-4
13. D. Zhao, X. Qian, X. Gu, S.A. Jajja, R. Yang, J. Electron. Packag. (2016). https://doi.org/10.1115/1.4034605
14. W. Capinski, H. Maris, Rev. Sci. Instrum. **67**, 2720 (1996). https://doi.org/10.1063/1.1147100
15. K. Chen, B. Song, N.K. Ravichandran, Q. Zheng, X. Chen et al., Science **367**, 555 (2020). https://doi.org/10.1126/science.aaz6149
16. C. Wei, X. Zheng, D. Cahill, J. Zhao, Rev. Sci. Instrum. **84**, 071301 (2013). https://doi.org/10.1063/1.4815867
17. J. Ravichandran, A.K. Yadav, R. Cheaito, P.B. Rossen, A. Soukiassian, S.J. Suresha, J.C. Duda, B.M. Foley, C.-H. Lee, Y. Zhu, A.W. Lichtenberger, J.E. Moore, D.A. Muller, D.G. Schlom, P.E. Hopkins, A. Majumdar, R. Ramesh, M.A. Zurbuchen, Nat. Mater. **13**, 168 (2014). https://doi.org/10.1038/nmat3826
18. F. Hofmann, M.P. Short, C.A. Dennett, MRS Bull. **44**, 392 (2019). https://doi.org/10.1557/mrs.2019.104

19. S. Middlemas, Z. Hua, V. Chauhan, W.T. Yorgason, R. Schley, A. Khanolkar, M. Khafizov, D. Hurley, J. Nucl. Mater. **528**, 151842 (2020). https://doi.org/10.1016/j.jnucmat.2019.151842
20. D.H. Olson, J.L. Braun, P.E. Hopkins, J. Appl. Phys. **126**, 150901 (2019). https://doi.org/10.1063/1.5120310
21. A.J. Schmidt, X. Chen, G. Chen, Rev. Sci. Instrum. **79**, 114902 (2008). https://doi.org/10.1063/1.3006335
22. D. Cahill, Rev. Sci. Instrum. **75**, 5119 (2004). https://doi.org/10.1063/1.1819431
23. J. Feser, J. Liu, D. Cahill, Rev. Sci. Instrum. **85**, 104903 (2014). https://doi.org/10.1063/1.4897622
24. C. Chiritescu, D. Cahill, N. Nguyen, D. Johnson, A. Bodapati, P. Keblinski, P. Zschack, Science **315**, 351 (2007). https://doi.org/10.1126/science.1136494
25. M. Li, J.S. Kang, Y. Hu, Rev. Sci. Instrum. **89**, 084901 (2018). https://doi.org/10.1063/1.5026028
26. A.J. Schmidt, R. Cheaito, M. Chiesa, Rev. Sci. Instrum. **80**, 094901 (2009). https://doi.org/10.1063/1.3212673
27. L. Tang, C. Dames, Int. J. Heat Mass Transf. **164**, 120600 (2021). https://doi.org/10.1016/j.ijheatmasstransfer.2020.120600
28. J. Malen, K. Baheti, T. Tong, Y. Zhao, J. Hudgings, A. Majumdar, J. Heat Trans. (2011). https://doi.org/10.1115/1.4003545
29. D. Hurley, R. Schley, M. Khafizov, B. Wendt, Rev. Sci. Instrum. **86**, 123901 (2015). https://doi.org/10.1063/1.4936213
30. Y. Wang, D.H. Hurley, E.P. Luther, M.F. Beaux, D.R. Vodnik, R.J. Peterson, B.L. Bennett, I.O. Usov, P. Yuan, X. Wang, M. Khafizov, Carbon **129**, 476 (2018). https://doi.org/10.1016/j.carbon.2017.12.041
31. J. Hartmann, P. Voigt, M. Reichling, J. Appl. Phys. **81**, 2966 (1997). https://doi.org/10.1063/1.364329
32. D. Fournier, M. Marangolo, C. Fretigny, J. Appl. Phys. **128**, 241101 (2020). https://doi.org/10.1063/5.0019025
33. J.L. Braun, D.H. Olson, J.T. Gaskins, P.E. Hopkins, Rev. Sci. Instrum. **90**, 024905 (2019). https://doi.org/10.1063/1.5056182
34. D. Hurley, O. Wright, O. Matsuda, S. Shinde, J. Appl. Phys. **107**, 023521 (2010). https://doi.org/10.1063/1.3272827
35. C. Cardell, I. Guerra, Trends Anal. Chem **77**, 156 (2016). https://doi.org/10.1016/j.trac.2015.12.001
36. K. Hatori, N. Taketoshi, T. Baba, H. Ohta, Rev. Sci. Instrum. **76**, 114901 (2005). https://doi.org/10.1063/1.2130333
37. A. Yarai, T. Nakanishi, Rev. Sci. Instrum. **78**, 054903 (2007). https://doi.org/10.1063/1.2736414
38. Raad, P. E.: Electronics Cooling Magazine (2008)
39. J. Liu, J. Zhu, M. Tian, X. Gu, A. Schmidt, R. Yang, Rev. Sci. Instrum. **84**, 034902 (2013). https://doi.org/10.1063/1.4797479
40. A.J. Schmidt, R. Cheaito, M. Chiesa, J. Appl. Phys. **107**, 024908 (2010). https://doi.org/10.1063/1.3289907
41. G. Langer, J. Hartmann, M. Reichling, Rev. Sci. Instrum. **68**, 1510 (1997). https://doi.org/10.1063/1.1147638
42. J.R. Rumble (ed.), *Handbook of Chemistry and Physics*, 99th edn. (CRC Press, Boca Raton, 2018)
43. P.E. Hopkins, P.M. Norris, R.J. Stevens, J. Heat Trans. (2008). https://doi.org/10.1115/1.2787025
44. M. Ahadi, M. Andisheh-Tadbir, M. Tam, M. Bahrami, Int. J. Heat Mass Transf. **96**, 371 (2016). https://doi.org/10.1016/j.ijheatmasstransfer.2016.01.037
45. Z. Hua, H. Ban, D.H. Hurley, Rev. Sci. Instrum. **86**, 054901 (2015). https://doi.org/10.1063/1.4919609
46. X. Zheng, D.G. Cahill, P. Krasnochtchekov, R.S. Averback, J.C. Zhao, Acta Mater. **55**, 5177 (2007). https://doi.org/10.1016/j.actamat.2007.05.037
47. D.R. Queen, F. Hellman, Rev. Sci. Instrum. **80**, 063901 (2009). https://doi.org/10.1063/1.3142463
48. B.C. Gundrum, D.G. Cahill, R.S. Averback, Phys. Rev. B **72**, 245426 (2005). https://doi.org/10.1103/PhysRevB.72.245426
49. Y.-J. Wu, L. Fang, Y. Xu, npj Comput. Mater. **5**, 56 (2019). https://doi.org/10.1038/s41524-019-0193-0
50. J. Yang, E. Ziade, A.J. Schmidt, Rev. Sci. Instrum. **87**, 014901 (2016). https://doi.org/10.1063/1.4939671
51. W. Shen, D. Vaca, S. Kumar, Nanosc. Microsc. Therm. **24**, 138 (2020). https://doi.org/10.1080/15567265.2020.1807662

52. P.R. Gadkari, A.P. Warren, R.M. Todi, R.V. Petrova, K.R. Coffey, J. Vac. Sci. Technol. A **23**, 1152 (2005). https://doi.org/10.1116/1.1861943